

## Atomic-scale quantification of charge densities in two-dimensional materials

Knut Müller-Caspary,<sup>1,2,3,\*</sup> Martial Duchamp,<sup>3,4</sup> Malte Rösner,<sup>5,6,7</sup> Vadim Migunov,<sup>3</sup> Florian Winkler,<sup>3</sup> Hao Yang,<sup>7</sup> Martin Huth,<sup>8</sup> Robert Ritz,<sup>8</sup> Martin Simson,<sup>8</sup> Sebastian Ihle,<sup>8</sup> Heike Soltau,<sup>8</sup> Tim Wehling,<sup>5,6</sup> Rafal E. Dunin-Borkowski,<sup>3</sup> Sandra Van Aert,<sup>1</sup> and Andreas Rosenauer<sup>2</sup>

<sup>1</sup>EMAT, Universiteit Antwerpen, Groenenborgerlaan 171, B-2020 Antwerpen, Belgium

<sup>2</sup>IFP, Universität Bremen, Otto-Hahn-Allee 1, 28359 Bremen, Germany

<sup>3</sup>Ernst Ruska-Centre for Microscopy and Spectroscopy with Electrons and Peter Grünberg Institute, Forschungszentrum Jülich, 52425 Jülich, Germany

<sup>4</sup>School of Materials Science and Engineering, Nanyang Technological University, 50 Nanyang Avenue, Singapore 639798, Singapore

<sup>5</sup>ITP, Universität Bremen, Otto-Hahn-Allee 1, 28359 Bremen, Germany

<sup>6</sup>BCCMS, Universität Bremen, Am Fallturm 1, 28359 Bremen, Germany

<sup>7</sup>Department of Physics and Astronomy, University of Southern California, Los Angeles, California 90089-0484, USA

<sup>8</sup>PNDetector GmbH, Otto-Hahn-Ring 6, 81739 München, Germany



(Received 9 May 2018; published 24 September 2018)

The charge density is among the most fundamental solid state properties determining bonding, electrical characteristics, and adsorption or catalysis at surfaces. While atomic-scale charge densities have as yet been retrieved by solid state theory, we demonstrate both charge density and electric field mapping across a mono-/bilayer boundary in 2D MoS<sub>2</sub> by momentum-resolved scanning transmission electron microscopy. Based on consistency of the four-dimensional experimental data, statistical parameter estimation and dynamical electron scattering simulations using strain-relaxed supercells, we are able to identify an AA-type bilayer stacking and charge depletion at the Mo-terminated layer edge.

DOI: [10.1103/PhysRevB.98.121408](https://doi.org/10.1103/PhysRevB.98.121408)

The discovery that mechanical, thermal, optical, and electrical properties of 2D materials such as graphene, Xenes (silicene, germanene), or transition metal dichalcogenides (TMDs, e.g., MoS<sub>2</sub>, WSe<sub>2</sub>) drastically differ from their bulk counterparts evoked enormous attention of both fundamental and applied research. The dominant route to get an atomistic understanding of bonding, conductance, band gaps, or photoluminescence spectra currently consists of setting up a structural model and performing *ab initio* simulations of the charge density, typically involving density functional theory [1–3] (DFT). Experimentally, electron microscopy can be used to provide atomically resolved structural data, e.g., by conventional scanning transmission electron microscopy (STEM) imaging at a spatial resolution down to 50 pm. However, an ultimate goal would be the direct observation of charge densities and electric fields at atomic resolution by electron microscopy at reasonable fields of view. Here, we take an important step towards this challenge by mapping these fundamental physical properties in 2D MoS<sub>2</sub> at atomic scale with a precision that allows for conclusions on, e.g., bilayer stacking.

This is now feasible as differential phase contrast [4–6] (DPC) STEM currently undergoes a rapid development from a classical, qualitative approach to quantitative electron picodiffraction [7,8] based on first moment detection [9]. The enhancement involves the acquisition of momentum-resolved STEM data, i.e., a 4D data set obtained by recording 2D

diffraction patterns for a probe scanning a 2D raster, which requires current ultrafast cameras [10–14] being capable of submillisecond frame times.

The physical background of our approach is summarized schematically in Fig. 1. The wave function of the incident STEM probe,  $\Psi_0$ , with amplitude (black) and phase (red) suffers a phase shift  $\exp(i\sigma V_P)$  by interacting with the projected Coulomb potential  $V_P$ ,  $\sigma = 0.01$  (V nm)<sup>-1</sup> being the interaction constant. Because the projected electric field  $\vec{E}_P = -\nabla V_P$  is not constant at the scale of the probe, the phase of the scattered wave is now curved. The deflection is measured in terms of the average lateral momentum transfer  $\langle \vec{p}_\perp \rangle$  from the first moment in diffraction patterns [7] with  $\perp$  indexing a plane perpendicular to the optical axis. Within the phase approximation, being valid for thin specimen, and accounting for partial spatial coherence of the electron source,  $\langle \vec{p}_\perp \rangle$  can be related to the projected electric field  $\vec{E}_P$  by Ehrenfest's theorem which results in [15]

$$\langle \vec{p}_\perp(\vec{R}) \rangle \frac{v}{-e} = [w \circ (\vec{E}_P * I_0)](\vec{R}) =: \vec{E}_m(\vec{R}). \quad (1)$$

Here,  $\vec{R}$  is the scan position,  $w$  describes the partial coherence of the electron source (typically Gaussian),  $I_0$  equals the normalized intensity of the incident probe,  $-e$  is the electron charge, and  $v$  its velocity. The measured electric field,  $\vec{E}_m$ , is thus directly proportional to the momentum transfer and represents the actual projected field  $\vec{E}_P$ , convolved (\*) with the probe intensity  $I_0$  and cross correlated ( $\circ$ ) with the source  $w$ . Note that these parameters determine the general lower limit for the spatial resolution in STEM. Furthermore, the measured

\*Corresponding author: [k.mueller-caspary@fz-juelich.de](mailto:k.mueller-caspary@fz-juelich.de)

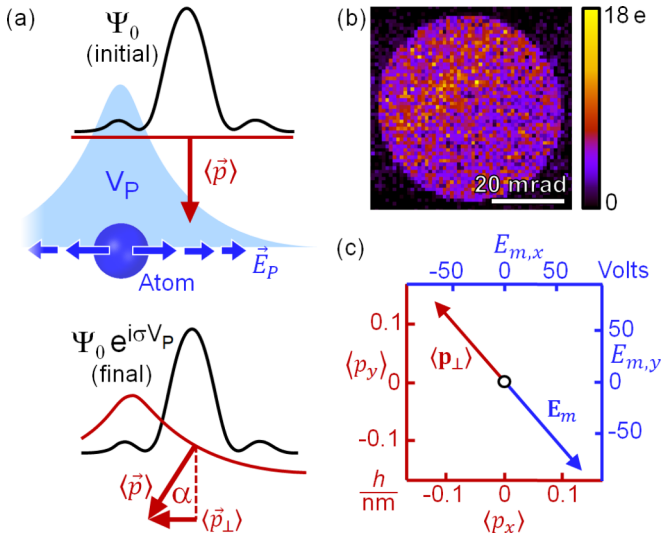


FIG. 1. Atomic electric field measurement. (a) Interaction of an electron wave (amplitude: black, phase: red) with the projected potential  $V_P$  and electric field  $\vec{E}_P$  of an atom. (b) Ronchigram acquired with 250  $\mu\text{s}$  frame time near a Mo site. The number of detected electrons is color coded. (c) Momentum transfer (red) and projected electric field  $\vec{E}_m$  (blue) determined from the Ronchigram in (c).

charge density  $\rho_m$  is obtained from Maxwell's equations,

$$\rho_m(\vec{R}) = \varepsilon_0 \text{div}_{\perp} \vec{E}_m(\vec{R}) = [w \circ (\rho_P * I_0)](\vec{R}), \quad (2)$$

and quantifies the projected charge density with the spatial resolution corresponding to the ultimate limit set by the microscope [15].

We used the pnCCD [10,14] camera with a frame rate of 4 kHz to record the central parts of the diffraction patterns (Ronchigrams) on a  $256^2$  STEM raster employing an aberration-corrected STEM instrument operated at 80 kV to avoid specimen damage [15]. Figure 1(b) depicts an example Ronchigram recorded close to a Mo atom. Although the electron fluence was kept low at approximately  $5.5 \times 10^5$  electrons/ $\text{\AA}^2$ , the redistribution of intensity due to the atomic electric field is obvious. Its first moment yields the momentum transfer  $\langle \vec{p}_{\perp} \rangle$  depicted in red in Fig. 1(c) with a modulus of  $0.18h \text{ nm}^{-1}$ . This corresponds to the measured electric field  $\vec{E}_m$  (blue) with a magnitude of 114 V calculated using Eq. (1). The momentum is given in units of Planck's constant  $h$  and the measured electric field in volts as it involves a projection operation through  $\vec{E}_P$ , according to Eq. (1).

Figure 2(a) depicts the atomically resolved electric field  $\vec{E}_m$  measured across an area of  $4 \times 4 \text{ nm}$ . This region is of particular interest because it contains a mono-/bilayer (ML/BL) boundary, as will be confirmed by simulations below. It is furthermore consistent with atom counting results using a statistics-based method [16–18] to evaluate scattering cross sections [15].

Field averages from the ML and BL have been calculated by a unit cell segmentation of the data and subsequent averaging involving a geometric transform as to the average cell geometry. The results are depicted in Fig. 2(b) with atomic sites indicated. Using Eq. (2), the charge density  $\rho_m$  in Fig. 2(c)

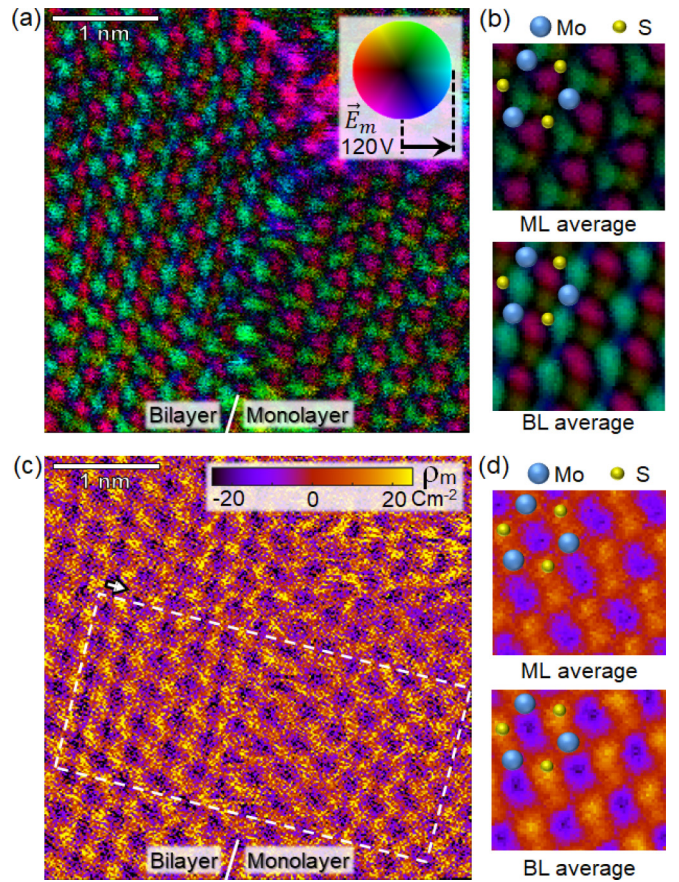


FIG. 2. Measured electric field and charge density in MoS<sub>2</sub>. (a) Color-coded electric field  $\vec{E}_m(\vec{R})$  of a mono-/bilayer (ML/BL) boundary with (b) unit cell averages. (c) Charge density  $\rho_m(\vec{R})$  calculated from (a) using Eq. (2) with the line profile region for Fig. 4(b) indicated (dashed rectangle). (d) Unit cell averages from (c).

was calculated from Fig. 2(a) with ML and BL averages in Fig. 2(d). In both the ML and the BL we observe the periodicity of the hexagonal MoS<sub>2</sub> lattice and individual atomic sites in Figs. 2(c) and 2(d). Note that the measured electric field vanishes at atomic sites as seen from the structural model imposed on the averaged cells in Fig. 2(b). This is reasonable because the measured field involves the convolution of the projected electric field  $\vec{E}_P$  with the probe intensity  $I_0$  [7].

Interestingly the electric fields in the ML and the BL look very similar concerning their shape as can be inferred from the color sequence around an atom, but the field magnitudes in the BL are higher. This points at a double-monolayer-type stacking referred to as AA [19] or 3R-like [20], as investigated below. The ML/BL edge region shows a different field distribution which is indicative for a particular edge termination determined hereafter. As to the charge density in Figs. 2(c) and 2(d) we find positive values at atomic sites owing to the (screened) nuclear charge surrounded by negative values because of the electronic contributions. In the boundary region the charge density variations appear weaker than in the ML or BL. We emphasize that both electric field and charge density are mapped directly, without input of structure or chemistry, in contrast to former studies [21–23]. Furthermore no complex reconstruction procedure is involved such as for ptychography

[24,25], and no field-free area for a reference wave is needed as is the case for holography [26].

The data of Fig. 2 is now investigated in more detail to explore whether the precision of our charge density mapping allows us to draw conclusions about the stacking sequence of the BL and the termination at the ML/BL edge, solely from the charge density results. To this end, supercells with different stacking sequences and edge terminations have been created, strain relaxed by DFT [2,3] and then used as an input for STEM multislice [27] simulations particularly accounting for partial spatial coherence and specimen tilt. The analysis of the stacking is presented in Fig. 3 with the different stacking configurations illustrated in (a), simulated electric fields in (b), and charge densities in (c). Added as a plausibility check, the ML simulation in Fig. 3 (top) is in remarkable quantitative agreement with its experimental counterparts in Figs. 2(b) and 2(d), bearing in mind that the color scales of Figs. 2 and 3 are identical. Note that the actual specimen tilt of  $7.5^\circ$  around the axis indicated in (b), top, was accounted for [15]. The stacking terminology was adopted from Ref. [19] with the Ramsdell notation in brackets where applicable.

The AB sequence for the BL stacking can immediately be rejected by comparison with Figs. 2(b) and 2(d). Distinguishing between AA and AA' is more challenging when considering only the electric fields. A more obvious decision is made from the charge densities in Fig. 3(c) of which the AA variant exhibits an asymmetric dumbbell similar to the experiment in Fig. 2(d) but contrary to the AA' stacking. The asymmetry becomes clear from the structural model since all atomic columns will have identical projected potentials for the AA' case. To illustrate this explicitly, Fig. 3(d) shows the integrated charge density profiles across the dumbbell marked by the dashed rectangles in Fig. 3(c). Indeed the AA stacking model represents the experimental data best concerning both the asymmetric character and the magnitude. Finally, Fig. 3(e) compiles simulation (insets) and experiment for both the ML and the AA-stacked BL at the same color scale, exhibiting perfect agreement within the experimental precision imposed by counting statistics.

The violation of inversion symmetry as seen from the projected charge density for the BL has important consequences on the optical properties. Since the AA-stacked bilayer can be considered a double monolayer, it exhibits twice the nonlinear susceptibility compared to a ML and shows strong spin- and valley selective circular dichroism [20]. However, the AA stacking is one variant among several others that have been observed, each constituting a local energetic minimum and unique optical properties [19,20,28]. That the present BL can take a stacking sequence that does not correspond to the global energetic minimum can be explained by the mechanical stress introduced during exfoliation and by the fact that the BL flake is kept fixed by surrounding (multi)layer steps or amorphous contamination.

Concerning the termination of the BL edge, Fig. 4(a) shows the sulfur dimer ( $S_2$ ), sulfur monomer ( $S_1$ ), and molybdenum monomer ( $Mo_1$ ) configurations. The differences become most obvious in average charge density profiles across the ML/BL boundary calculated in the region indicated by the dashed rectangle in Fig. 2(c). Experimentally, a charge density oscillation of up to  $\pm 9 \text{ cm}^{-2}$  in the BL and  $\pm 6.5 \text{ cm}^{-2}$

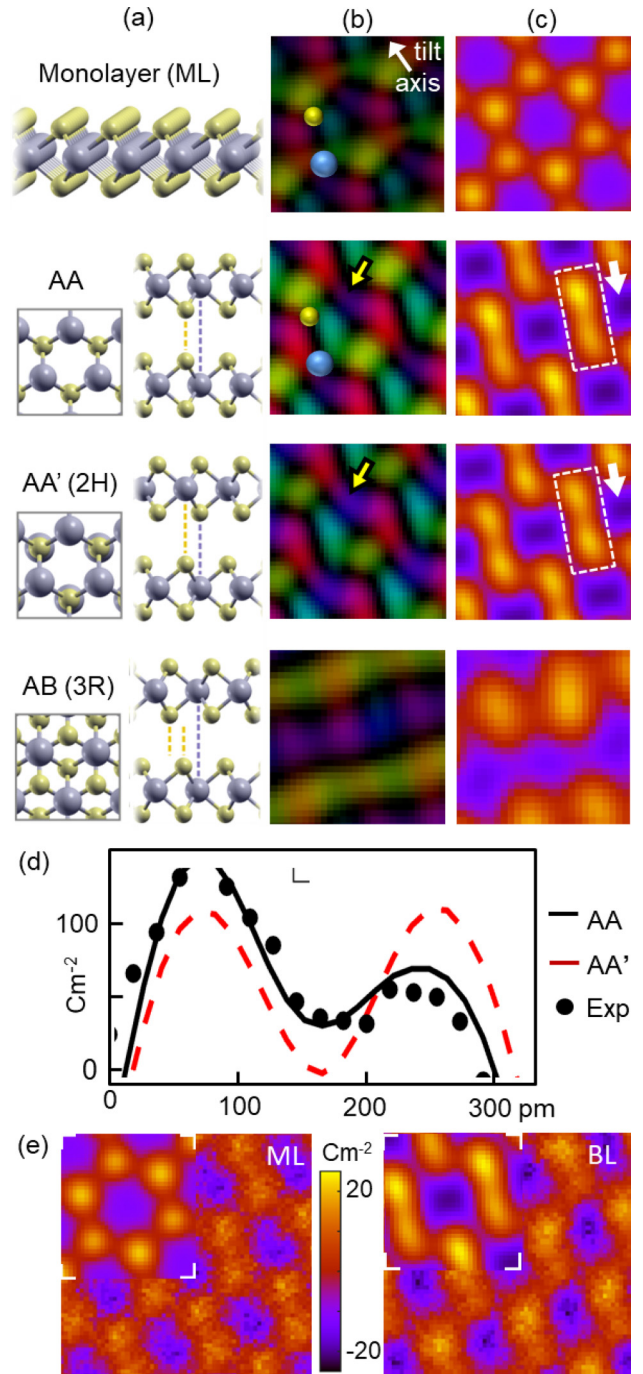


FIG. 3. Simulated electric fields and charge densities. (a) Models for the monolayer (ML) and bilayer stackings. (b) Electric field corresponding to (a) with distinguishing features marked by the yellow arrow. A tilt of  $7.5^\circ$  around the axis indicated [(b), top] was determined from the experimental data. (c) Charge densities derived from (b). Color legends of (b) and (c) are equal to Fig. 2. (d) Integrated charge density profiles taken in (c) (dashed rectangle) and the equivalent region in Fig. 2(d). (e) Simulation (insets) and unit cell averages superimposed for the ML and the AA-stacked BL.

in the ML are observed as shown at the top of Fig. 4(b). Interestingly, it drops to  $[-4.5 \dots 3] \text{ cm}^{-2}$  at the edge. The three simulated counterparts drawn at the bottom of Fig. 4(b) have been obtained by STEM multislice [27] simulations

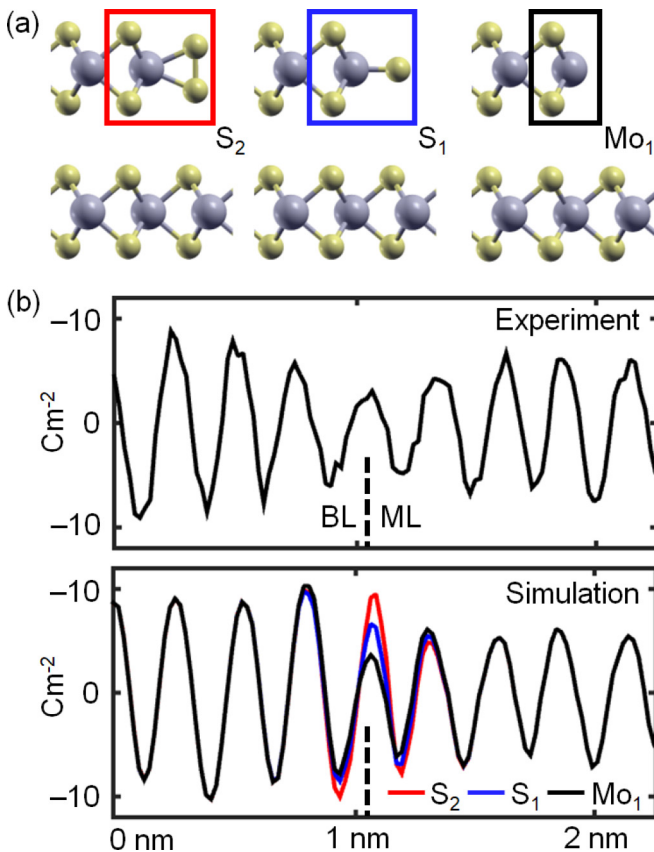


FIG. 4. Termination of the MoS<sub>2</sub> ML/BL edge. (a) Strain-minimized edge models used for the multislice simulations. (b) Experimental (top) charge density profile taken in the dashed region of Fig. 2(c). Below the simulated analogons are shown for the models in (a), indicating a Mo<sub>1</sub> termination.

using the experimental parameters and the structures from Fig. 4(a). The measured charge depletion is only observed for an edge terminated by a Mo monomer (black). How-

ever, simulation and experiment match nearly perfectly safely inside the ML/BL, while the Mo<sub>1</sub> simulation exhibits still slightly too high charge densities near the edge. This might be attributed to strain which is not taken into account in the simulation. In terms of Pythagorean sums of the differences to the experimental profile per pixel, we find 0.031, 0.024, and 0.021 cm<sup>-2</sup> for the S<sub>2</sub>, S<sub>1</sub>, and Mo<sub>1</sub> cases, respectively, so that the Mo termination is the most likely edge configuration. This demonstrates that this technique can be very valuable in future studies where the charge density is to be correlated, e.g., with catalytic or electrical properties. For example, Mo edges were found catalytically active [29,30] and exhibit metallic character [31] aside from the semiconducting nature of MoS<sub>2</sub>.

To conclude, distinguishing features of an AA-stacked MoS<sub>2</sub> bilayer could be resolved by means of atomic-scale electric field and charge density mapping, which exhibit a violation of inversion symmetry. The assignment of a Mo termination to the mono-/bilayer edge, accompanied by a depleted charge density, demonstrates the sensitivity of the method. The presented study shows great promise to shed light on the atomic-scale electrical configuration of vacancies, dopant atoms, dislocations, stacking faults, and multilayer stacking in the growing family of 2D materials. Enhancing the precision further so as to be sensitive to bonding effects will surely dominate upcoming work, for which low-Z 2D materials such as N-doped graphene or BN would be interesting applications.

This concurrence of excellent momentum resolution, the quantum mechanical interpretation of 4D experimental data, aberration-corrected low-voltage STEM, and ultrafast electron detectors is fundamentally changing the scope of atomic-resolution solid state research, now allowing for atomic-scale charge density mapping without any prior knowledge of atomic species or sites.

K.M.-C. acknowledges funding from the Initiative and Network Fund of the Helmholtz Association (VH-NG-1317) within the framework of the Helmholtz Young Investigator Group *moreSTEM* at Forschungszentrum Jülich, Germany.

- [1] P. Blaha, K. Schwarz, P. Sorantin, and S. Trickey, *Comput. Phys. Commun.* **59**, 399 (1990).
- [2] G. Kresse and J. Furthmüller, *Comput. Mater. Sci.* **6**, 15 (1996).
- [3] G. Kresse and J. Hafner, *Phys. Rev. B* **47**, 558 (1993).
- [4] N. H. Dekkers and H. de Lang, *Optik* **41**, 452 (1974).
- [5] H. Rose, *Ultramicroscopy* **2**, 251 (1977).
- [6] N. Shibata, S. D. Findlay, Y. Kohno, H. Sawada, Y. Kondo, and Y. Ikuhara, *Nat. Phys.* **8**, 611 (2012).
- [7] K. Müller, F. F. Krause, A. Beche, M. Schowalter, V. Galioit, S. Löffler, J. Verbeeck, J. Zweck, P. Schattschneider, and A. Rosenauer, *Nat. Commun.* **5**, 5653 (2014).
- [8] K. Müller-Caspary, F. F. Krause, T. Grieb, S. Löffler, M. Schowalter, A. Béché, V. Galioit, D. Marquardt, J. Zweck, P. Schattschneider, J. Verbeeck, and A. Rosenauer, *Ultramicroscopy* **178**, 62 (2017).
- [9] E. M. Waddell and J. N. Chapman, *Optik* **54**, 83 (1979).
- [10] K. Müller, H. Ryll, I. Ordavo, S. Ihle, L. Strüder, K. Volz, J. Zweck, H. Soltau, and A. Rosenauer, *Appl. Phys. Lett.* **101**, 212110 (2012).
- [11] V. B. Ozdol, C. Gammer, X. G. Jin, P. Ercius, C. Ophus, J. Ciston, and A. M. Minor, *Appl. Phys. Lett.* **106**, 253107 (2015).
- [12] K. Müller-Caspary, A. Oelsner, and P. Potapov, *Appl. Phys. Lett.* **107**, 072110 (2015).
- [13] M. W. Tate, P. Purohit, D. Chamberlain, K. X. Nguyen, R. Hovden, C. S. Chang, P. Deb, E. Turgut, J. T. Heron, D. G. Schlom, D. C. Ralph, G. D. Fuchs, K. S. Shanks, H. T. Philipp, D. A. Muller, and S. M. Gruner, *Microscopy and Microanalysis* **22**, 237 (2016).
- [14] H. Ryll, M. Simson, R. Hartmann, P. Holl, M. Huth, S. Ihle, Y. Kondo, P. Kotula, A. Liebel, K. Müller-Caspary, A. Rosenauer, R. Sagawa, J. Schmidt, H. Soltau, and L. Strüder, *J. Instrum.* **11**, P04006 (2016).

- [15] See Supplemental Material at <http://link.aps.org/supplemental/10.1103/PhysRevB.98.121408> for the mathematical treatment of partial spatial coherence, experimental and simulation details, simulation studies of focus dependence, spatial coherence, and the validity of the phase approximation.
- [16] S. Van Aert, K. J. Batenburg, M. D. Rossell, R. Erni, and G. Van Tendeloo, *Nature (London)* **470**, 374 (2011).
- [17] S. Van Aert, A. De Backer, G. T. Martinez, B. Goris, S. Bals, G. Van Tendeloo, and A. Rosenauer, *Phys. Rev. B* **87**, 064107 (2013).
- [18] A. D. Backer, K. van den Bos, W. V. den Broek, J. Sijbers, and S. V. Aert, *Ultramicroscopy* **171**, 104 (2016).
- [19] J. He, K. Hummer, and C. Franchini, *Phys. Rev. B* **89**, 075409 (2014).
- [20] T. Jiang, H. Liu, D. Huang, S. Zhang, Y. Li, X. Gong, Y.-R. Shen, W.-T. Liu, and S. Wu, *Nat. Nanotechnol.* **9**, 825 (2014).
- [21] J. M. Zuo, J. C. H. Spence, and M. O’Keeffe, *Phys. Rev. Lett.* **61**, 353 (1988).
- [22] K. Tsuda, Y. Ogata, K. Takagi, T. Hashimoto, and M. Tanaka, *Acta Crystallogr. Sect. A* **58**, 514 (2002).
- [23] J. C. Meyer, S. Kurasch, H. J. Park, V. Skakalova, D. Künzel, A. Groß, A. Chuvilin, G. Algara-Siller, S. Roth, T. Iwasaki, U. Starke, J. H. Smet, and U. Kaiser, *Nat. Mater.* **10**, 209 (2011).
- [24] H. Yang, R. N. Rutte, L. Jones, M. Simson, R. Sagawa, H. Ryll, M. Huth, T. J. Pennycook, M. L. H. Green, H. Soltau, Y. Kondo, B. G. Davis, and P. D. Nellist, *Nat. Commun.* **7**, 12532 (2016).
- [25] S. Gao, P. Wang, F. Zhang, G. T. Martinez, P. D. Nellist, X. Pan, and A. I. Kirkland, *Nat. Commun.* **8**, 163 (2017).
- [26] P. A. Midgley and R.-E. Dunin-Borkowski, *Nat. Mater.* **8**, 271 (2009).
- [27] A. Rosenauer and M. Schowalter, in *Springer Proceedings in Physics*, edited by A. G. Cullis and P. A. Midgley (Springer, Dordrecht, 2007), Vol. 120, pp. 169–172.
- [28] M. Xia, B. Li, K. Yin, G. Capellini, G. Niu, Y. Gong, W. Zhou, P. M. Ajayan, and Y.-H. Xie, *ACS Nano* **9**, 12246 (2015).
- [29] C. Kisielowski, Q. Ramasse, L. Hansen, M. Brorson, A. Carlsson, A. Molenbroek, H. Topsøe, and S. Helveg, *Angewandte Chemie International Edition* **49**, 2708 (2010).
- [30] F. Besenbacher, M. Brorson, B. S. Clausen, S. Helveg, B. Hinnemann, J. Kibsgaard, J. Lauritsen, P. Moses, J. Nørskov, and H. Topsøe, *Catal. Today* **130**, 86 (2008).
- [31] M. V. Bollinger, J. V. Lauritsen, K. W. Jacobsen, J. K. Nørskov, S. Helveg, and F. Besenbacher, *Phys. Rev. Lett.* **87**, 196803 (2001).